

RESEARCH ARTICLE

[View Article Online](#)
[View Journal](#) | [View Issue](#)



Cite this: *Mater. Chem. Front.*,
2022, 6, 3042

Isoquinolinium-based photosensitizers with aggregation-induced emission characteristics for highly efficient photodynamic combat of viruses[†]

Meijia Gu,[‡]^a Ming-Yu Wu,  Yuncong Yuan,^d Po-Yu Ho,^b Zhou Zhou,^d Engui Zhao,  Chao Shen^{*d} and Sijie Chen 

Because of the prevalence of COVID-19, people are becoming increasingly aware of the importance of disinfection, which necessitates the development of convenient and efficient methods for inactivating pathogens. In this work, we report the application of three isoquinolinium-based aggregation-induced-emission-active photosensitizers (PSs) for photodynamic inactivation (PDI) of viruses at a low light intensity of 9 mW cm^{-2} . These three PSs could highly efficiently sensitize the production of reactive oxygen species and are applied to PDI of viruses. Their inactivation effects on viruses are evaluated by checking the cytopathic effect through examining the morphology of their host cells, investigating their protein expression in host cells by Western blot, immunofluorescence imaging of the viral proteins in host cells, quantifying the viral RNA levels after infection, and viral titering-median tissue culture infectious dose (TCID₅₀) assay. The experimental results obtained clearly demonstrate the excellent PDI effect of these three PSs on viruses. Besides, we also explore the feasibility of employing these PSs for PDI of viruses on simulated high-touch surfaces, such as stainless steel and glass slides, on which these PSs demonstrate an even better PDI effect on all the three tested viruses. The PDI method described in this work is expected to innovate the disinfection practice in public areas.

Received 1st July 2022,
Accepted 18th August 2022

DOI: 10.1039/d2qm00630h

rsc.li/frontiers-materials

Introduction

COVID-19 is undoubtedly the worst pandemic in human history with more than 535.8 million confirmed cases and over 6.3 million deaths (data from WHO on 17 June 2022).^{1–3} The wide spread of COVID-19 arises from its high infectivity.⁴ The development of convenient and efficient methods for virus inactivation has come back to the spotlight.⁵ Research has revealed that viruses, such as severe acute respiratory syndrome (SARS) coronavirus, Middle East respiratory syndrome (MERS)

coronavirus and endemic human coronavirus (HCoV), can survive for up to 9 days on inanimate surfaces such as metal, glass or plastic.⁶ Though 75% alcohol and hypochlorite are effective agents for inactivation of viruses, they can easily evaporate or be inactivated.⁷ Thus, they work well for disinfecting contaminated surfaces, but new microbes could still adhere to the surface and remain active to infect other people until the next disinfection practice. Their protection performance mostly depends on the frequency of applying these disinfectants. Therefore, efficient methods for continuously inactivating viral pathogens and preventing the spread of infectious pathogens in a variety of public places, such as hospitals, public transportation and schools, are in urgent need.^{8–10}

Photodynamic inactivation (PDI) is a noninvasive therapeutic strategy for the combat of microbe infections.^{11,12} In PDI, photosensitizers (PSs) and light illumination are utilized to generate cytotoxic reactive oxygen species (ROS), which can cause oxidative damage to membrane lipids, nucleic acids, and proteins and induce the death of pathogens. With the superiority of limited antibiotic resistance, low systemic toxicity, and high specificity, PDI has attracted increasing attention.^{13–15}

In practical PDI applications, PSs are usually utilized at high concentrations or fabricated into films and subjected to constant irradiation for continuous inactivation of pathogens.

^a Key Laboratory of Combinatorial Biosynthesis and Drug Discovery, Ministry of Education, School of Pharmaceutical Sciences, Wuhan University, Wuhan 430071, Hubei, China

^b Ming Wai Lau Centre for Reparative Medicine, Karolinska Institutet, Hong Kong 999077, China. E-mail: sijie.chen@ki.se

^c Sichuan Engineering Research Center for Biomimetic Synthesis of Natural Drugs, School of Life Science and Engineering, Southwest Jiaotong University, Chengdu 610031, China

^d College of Life Sciences, Wuhan University, Wuhan 430072, Hubei, China. E-mail: shenchao@whu.edu.cn

^e School of Science, Harbin Institute of Technology, Shenzhen, HIT Campus of University Town, Shenzhen 518055, China. E-mail: zhaoengui@hit.edu.cn

[†] Electronic supplementary information (ESI) available. See DOI: <https://doi.org/10.1039/d2qm00630h>

[‡] These two authors contributed equally to this work.



Thus, good photostability and high ROS sensitizing efficiency are of crucial importance.^{16–18} To increase the photostability and ROS sensitizing efficiency, increasing the concentration of PSs is the intuitive method that we can come up with. However, most PSs are derived from conventional fluorogens with planar conjugated structures. These fluorogens suffer from the aggregation-caused quenching (ACQ) effect, with bright fluorescence in dilute solutions but weakened or completely quenched fluorescence at high working concentrations or in the aggregated state, due to the strong π – π stacking interactions.¹⁹ Along with fluorescence quenching at high concentrations is the decrease in the ROS sensitizing efficiency, due to the high nonradiative decay rate caused by π – π stacking interactions. Thus, traditional PSs can only work well in solutions and at low concentrations, which limits their practical applications.^{20–23}

In 2001, Prof. Tang proposed the concept of aggregation-induced emission (AIE) after observing the opposite effect to ACQ: AIE molecules emit faintly in solution, but fluoresce

intensely in the aggregated state.^{24–29} Further investigations revealed that they could also highly efficiently sensitize the production of ROS in the aggregated state and were thus applied to photodynamic therapy of tumors and PDI of bacteria and fungi.^{30–33} In contrast, AIE-based PSs have seldom been applied to the PDI of viruses.^{34–36}

Isoquinolinium-based AIE-active photosensitizers demonstrated high ROS sensitizing efficiency, large Stokes shift, good photostability and ease of synthesis, and were applied to photodynamic anticancer and antibacterial therapies.^{37–41} Previously, we developed three isoquinolinium-based AIE PSs (TPE-IQ, TPE-IQ-2O and LIQ-TPE, Fig. 1a) through a simple Rh-catalysed annulation reaction with high yields.^{42–44} These PSs showed high ROS sensitizing efficiencies and demonstrated excellent performance in photodynamic anticancer and anti-biosis. The lipophilic cations of these isoquinoliniums are beneficial for binding with phospholipid bilayers or protein covering their capsid, and therefore they are able to destroy the

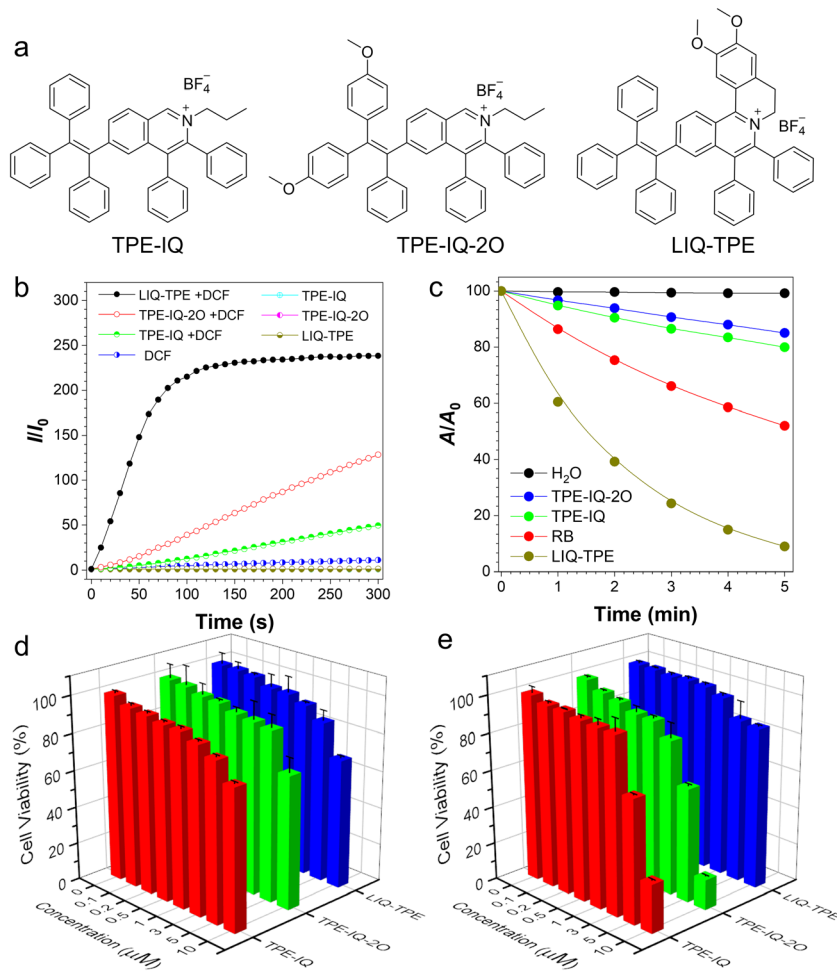


Fig. 1 (a) Molecular structures of TPE-IQ, TPE-IQ-2O and LIQ-TPE. (b) Investigations on the ROS sensitizing ability of TPE-IQ, TPE-IQ-2O and LIQ-TPE upon white-light irradiation. Relative changes in fluorescence intensity (I/I_0) at 534 nm of LIQ-TPE (2.5 μ M), TPE-IQ-2O (2.5 μ M), TPE-IQ (2.5 μ M), DCF (2.5 μ M) and mixtures of DCF with LIQ-TPE, TPE-IQ-2O, and TPE-IQ in water upon white-light irradiation for different times. (c) Decomposition rates of ABDA in the absence or presence of RB, TPE-IQ, TPE-IQ-2O or LIQ-TPE under white-light irradiation (20 mW cm^{-2}), where A_0 and A are the initial absorbance and final absorbance of ABDA at 378 nm. (d) and (e) Biocompatibility of TPE-IQ, TPE-IQ-2O and LIQ-TPE evaluated by the CCK-8 assay in (d) MRC-5 cells and (e) BHK-21 cells after incubation for 24 h.



lipid or protein of virus under light irradiation.³⁶ Herein, in this work, we employed TPE-IQ, TPE-IQ-2O and LIQ-TPE for highly efficient photodynamic combat of viruses. All these three PSs can efficiently inactivate, and thus prevent the spread of viruses. The antiviral performance was supported by the significantly decreased RNA copies in qPCR analysis, reduced levels of virus proteins evaluated by Western blot and immunofluorescence imaging, and decreased median tissue culture infectious dose (TCID₅₀) in viral titering. Furthermore, these three PSs demonstrated effective antiviral performances on simulated high-touch surfaces such as glass and metal, indicating their great potential in preventing the spread of infectious viruses.

Experimental

Materials and general instruments

The CCK-8 kit was purchased from MedChemExpress. The minimum essential medium (MEM) was purchased from Gibco. Phosphate buffered saline (PBS), penicillin and streptomycin were purchased from Invitrogen. Dulbecco's modified Eagle's medium (DMEM), fetal bovine serum (FBS), and trypsin-EDTA were purchased from Thermo Fisher Scientific. The FMDV 3D protein rabbit primary antibody, HCoV-OC43 N rabbit primary antibody and HCoV-229E spike glycoprotein (S) rabbit primary antibody were customized and obtained from ABIOCENTER (Beijing, China). TRITC goat anti-mouse IgG (H+L) (AS026) and FITC goat anti-rabbit IgG (H+L) (AS011) were purchased from ABclonal (Wuhan, China). Goat anti-rabbit IgG (H+L) HRP (S0001) was obtained from Affinity Biosciences (Jiangsu, China). The antibody against HCoV-OC43 strain (MAB9012) was purchased from Millipore (US). The anti-GAPDH recombinant rabbit monoclonal antibody was bought from HuaBio (Hangzhou, China). Milli-Q water was supplied using a Milli-Q Plus System (Millipore Corporation, United States). Fluorescence images were collected using an Olympus IX71 inverted fluorescence microscope.

Cell and virus culture

The human embryonic lung fibroblast cell line (MRC-5) and baby hamster kidney cell line (BHK-21) were provided by the China Center for Type Culture Collection. MRC-5 and BHK-21 cells were cultured in the MEM supplemented with 10% fetal bovine serum (ExCell), 100 units mL⁻¹ penicillin and 100 µg mL⁻¹ streptomycin in a 5% CO₂ humidity incubator at 37 °C. One day before the infection experiment, the cells were seeded into a 24-well cell culture plate to approximately 70–80% confluence and then infected with the viruses.

FMDV serotype O viral strain (Akesu/58/2002, GenBank accession no. AF511039) was supplied by the Lanzhou Veterinary Research Institute, Chinese Academy of Agriculture Sciences. Human coronaviruses HCoV-229E (ATCC® VR-740) and HCoV-OC43 (ATCC® VR-1558) were purchased from the American Type Culture Collection, MD, USA. Cells were used to propagate viral stocks and measure viral titers by median tissue culture infectious dose (TCID₅₀) assays.

In a typical experiment, 2 µL of a 10 mM stock solution of TPE-IQ, TPE-IQ-2O or LIQ-TPE in DMSO was diluted to 1 mL with a cell culture medium, followed by further dilution to desired concentrations. After mixing with the PS, each well of viruses was incubated with the PS for 20 min, followed by exposure to white light (9 mW cm⁻²) or storage in the dark for 20 min.

CCK-8 assay for the determination of cell cytotoxicity

The cytotoxicity on cells was determined by the standard WST-8 (2-(2-methoxy-4-nitrophenyl)-3-(4-nitrophenyl)-5-(2,4-disulfophenyl)-2H-tetrazolium, monosodium salt) (CCK-8) assay. MRC-5 and BHK-21 cells were seeded at a density of 7 × 10³ cells per well in 96-well black microplates with 100 µL of the culture medium and cultured overnight to reach 70–80% confluence. After this, the medium was replaced with 100 µL of the fresh medium containing different concentrations of TPE-IQ, TPE-IQ-2O or LIQ-TPE (0, 0.1, 0.2, 0.5, 1.0, 3.0, 5.0, and 10 µM), and DMSO was used as a vehicle control. After 24 h of incubation, 10 µL of the 12 mM CCK-8 stock solution mixed with 90 µL of phosphate-buffered saline was added to each well for an additional 4 h of incubation. The absorbance was measured at 450 nm using a SpectraMax M2 microplate reader (molecular devices). The cell viability (%) was calculated as (OD₄₅₀ sample/OD₄₅₀ control) × 100%.

Viral infectivity assay

To characterize the PDI efficiency of PSs on viruses, host cells were infected with FMDV, HCoV-OC43 or HCoV-229E separately, and replication was determined by qPCR later. In brief, an equal number of cells were plated in 24-well plates. When cells reached 70–80% confluence, they were infected with FMDV, HCoV-OC43 or HCoV-229E at a virus concentration of 2.5 × 10⁻⁴ PFU per cell. After 24 hours, morphological changes were observed under an Olympus IX71 inverted fluorescence microscope.

RNA extraction and real-time quantitative polymerase chain reaction (qPCR)

After viral infection, cells were collected and RNAs were extracted using the TRIzol reagent (Thermo Fisher Scientific) according to the manufacturer's protocol. The integrity and purity of RNAs were tested using 1.5% agarose gels, NANO DROP2000 (Thermo), and Agilent 2100. cDNA synthesis was performed according to standard protocols. Briefly, 1 µg of RNA was reverse-transcribed using an Oligo(dT)15 Primer (Takara) and M-MLV reverse transcriptase (Promega) with RNase inhibitors (Takara). First, 1 µL of the oligo(dT)15 primer (10 µM) was added into the RNAs with a denaturation step at 70 °C for 5 min, followed by mixing evenly with the reverse transcription reaction mixture as follows: 0.5 µL of M-MLV reverse transcriptase (Promega), 4 µL of 5× reaction buffer, 2 µL of dNTP (10 mM), 1 µL of RNase inhibitor (Takara), and H₂O to a final volume of 20 µL. The reverse transcription reaction was then performed at 42 °C for 60 min and enzyme deactivation at 70 °C for 15 min.

Primers of qPCR were designed with Primer Premier 6.0 software (Primer, Canada). The qPCR primers used are listed in Table S1 (ESI†). Each qPCR reaction mixture contained 5 µL of



the first-strand cDNA from the RT-PCR, 10 μ L of 2 \times Taq Pro Universal SYBR qPCR Master Mix (Vazyme Biotech), 0.5 μ L of each primer (25 μ M), and 4 μ L of RNase free H₂O to a final volume of 25 μ L. The amplification reaction was achieved through one denaturation cycle at 95 °C for 10 min followed by 40 cycles at 94 °C for 30 s, 58 °C for 30 s and a final extension cycle at 72 °C for 20 s in the CFX96TM RT-PCR detection system (BIO-RAD). *GAPDH* was chosen as a reference gene to normalize the gene expression levels, and the results were analyzed using the $2^{-\Delta\Delta Ct}$ method.

Each sample was subjected to three independent replicates. All assays were performed with three independent biological replicates. Data analyses were performed using Rotor-Gene 4.6.

Immunofluorescence

Cells grown in 24-well plates were washed twice with PBS and fixed with 4% paraformaldehyde for 30 min followed by permeabilization with 0.5% Triton-X 100 for 15 min. After washing twice with PBS, 5 min each, at room temperature, the cells were blocked with 5% bovine serum albumin for 30 min. The cells were then incubated with FMDV 3D rabbit pAb (1:50), anti-coronavirus mouse antibody (1:100) or HCoV-229E spike glycoprotein (S) rabbit pAb (1:50) overnight at 4 °C. Then the cells were washed with PBS three times, 5 min each, and incubated with the corresponding secondary antibody FITC goat anti-rabbit IgG (H+L) (1:200) (Acloneal) or TRITC goat anti-mouse IgG (H+L) (1:200) for 2 h at room temperature. Finally, the cells were washed three times with PBS and observed using an Olympus IX71 inverted fluorescence microscope coupled with cellSens software.

Western blot analysis

Cells in different groups were washed twice with PBS and proteins were extracted with 2 \times SDS buffer and then boiled for 5 min. After centrifugation for 10 min at 10 000 \times g, the supernatant was subjected to electrophoresis with a 10% SDS-PAGE gel followed by electrotransferring onto a polyvinylidene fluoride (PVDF) membrane (Bio-Rad) for Western blot analysis. Prior to the detection of target proteins with a specific protein antibody, the transferred membranes were blocked with 5% skim milk (BD Biosciences) for 1 h at room temperature to reduce non-specific binding. Excess milk was washed away three times, and immunoblotting was performed with the FMDV 3D protein antibody (1:2000), HCoV-OC43 N protein antibody (1:2000), HCoV-229E spike glycoprotein (S) antibody (1:2000), or GAPDH protein antibody (1:5000) followed by the HRP-conjugated goat anti-rabbit IgG (H+L) secondary antibody (1:5000) to develop the blotting results. After washing three times with TBST (containing 0.15% Tween-20), membrane-bound antibodies were detected using the Immobilon Western Chemiluminescent HRP substrate. The results were presented using the GelDoc XR System (Bio-Rad), and all experiments were repeated independently three times.

TCID₅₀ assays

MRC-5 cells were incubated in 96-well plates at a concentration of 5000 cells per well, and the cells could be used for TCID₅₀

when the confluence reached over 70%. And the virus stock solution was diluted with a 10-fold gradient. The dilution factors for FMDV and HCoV-OC43 were from 10¹ to 10⁶ and from 10¹ to 10⁵, respectively. Afterwards, the supernatants in the 96-well plate were discarded, and 100 μ L per well of virus diluents were added to the 96-well plate. For each dilution, 8 parallel wells were prepared. The MEM was used as the negative control. Then the infection of viruses was performed under 5% CO₂ at 37 °C. The cytopathic effect of MRC-5 cells was observed after diluted viruses were added to 96-well plates for 3 days, and the numbers of CPE positive wells at each dilution were counted. The titers of viruses were calculated according to the Reed-Muench calculation method.

PDI of viruses on stainless steel or glass slides

Sterilized iron and glasses with an area of 1 cm² were randomly divided into control groups and experimental groups with three independent replicates. Different concentrations of TPE-IQ, TPE-IQ-2O or LIQ-TPE (12 μ L) in ethanol were added onto stainless steel or glass slides to completely immerse the substrate. After air-drying for more than 12 h, the substrates were placed in 24-well plates and incubated with FMDV, HCoV-OC43 or HCoV-229E for 20 min, and then treated without/with white-light irradiation (9 mW cm⁻²) for 20 min. The BHK-21 cells and MRC-5 cells were infected with FMDV, and HCoV-OC43/HCoV-229E for 24 h, respectively. The replications were then determined by the qPCR. In brief, an equal number of cells were plated in 24-well plates. When cells reached 70–80% confluence, they were infected with FMDV, HCoV-OC43 or HCoV-229E. After 24 hours, cells were collected and RNA was extracted with the TRIzol reagent (Thermo Fisher Scientific) according to the manufacturer protocol, followed by the qPCR analysis of RNA copies.

Results and discussion

ROS sensitizing efficiency of TPE-IQ, TPE-IQ-2O and LIQ-TPE

For PDI applications, high ROS sensitizing efficiency is beneficial for achieving a good therapeutic effect. TPE-IQ, TPE-IQ-2O and LIQ-TPE with AIE attributes formed nanoparticles in PBS with average diameters of 258.0 nm, 222.9 nm and 202.1 nm, respectively (Fig. S1, ESI†), which were beneficial for sensitizing ROS production.⁴⁵ We thus evaluated the ROS sensitizing efficiency of TPE-IQ, TPE-IQ-2O and LIQ-TPE by using a widely used fluorescent sensor, DCF, as an indicator. As shown in Fig. 1b, TPE-IQ, TPE-IQ-2O, LIQ-TPE or DCF alone showed no or low fluorescence intensity at 534 nm, which remained almost unchanged upon irradiation with white light (20 mW cm⁻²) for up to 300 s. In contrast, in the presence of the three isoquinolinium-based AIE-active PSs and DCF, a gradual increase in the fluorescence intensity at 534 nm was observed in all the three PSs with prolonged exposure to white-light irradiation. The fluorescence intensities were increased by 49.6-, 128.5- and 238.4-fold after 300 s irradiation for TPE-IQ, TPE-IQ-2O and LIQ-TPE, respectively, indicative of their high ROS sensitizing efficiency.



Next, the $^1\text{O}_2$ sensitizing abilities of these three isoquinolinium-based PSs were studied by measuring changes in the absorption spectra of the $^1\text{O}_2$ indicator, 9,10-anthracenediyl-bis(methylene) dimalonic acid (ABDA), under white-light irradiation (20 mW cm^{-2}). As illustrated in Fig. 1c and Fig. S2 (ESI[†]), the absorbances of ABDA (50 mM) at 378 nm in the solution containing PSs (2.5 μM) were decreased to 85% (TPE-IQ), 80% (TPE-IQ-2O) and 8.9% (LIQ-TPE) of their original levels gradually upon white-light irradiation for 5 min. However, the absorption profile of the ABDA solution was almost not changed under the same experimental conditions without PSs. These results clearly demonstrated that all these three PSs could efficiently sensitize the generation of $^1\text{O}_2$ for PDI. For comparison, the ROS sensitizing efficiency of a widely used PS, Rose Bengal (RB), was also evaluated. Under the same experimental conditions, the absorbance of ABDA at 378 nm in solution containing 2.5 μM RB only decreased to 52% of its original value. Among these three PSs, LIQ-TPE showed the highest ROS photosensitizing efficiency and best $^1\text{O}_2$ sensitizing abilities and its performance was superior to RB. The superb singlet oxygen sensitizing performance of LIQ-TPE could be partially ascribed to its longer absorption band and higher extinction coefficient than those of TPE-IQ and TPE-IQ-2O (Fig. S3, ESI[†]). Besides, higher singlet oxygen quantum efficiency is another crucial factor contributing to its excellent singlet oxygen sensitizing performance.

Cytotoxicity of TPE-IQ, TPE-IQ-2O and LIQ-TPE

The cytotoxicity of TPE-IQ, TPE-IQ-2O and LIQ-TPE was evaluated by employing the cell counting kit-8 (CCK-8) method in the human fetal lung fibroblast (MRC-5) (Fig. 1d) and baby hamster kidney fibroblast (BHK-21) cells (Fig. 1e). Generally speaking, these three PSs showed lower cytotoxicity on MRC-5 cells than that on BHK-21 cells. These three PSs were friendly to both MRC-5 cells and BHK-21 cells at concentrations of lower than 3 μM with more than 82% cell survival after 24 h incubation. At a PS concentration of 5 μM , 85% MRC-5 cells survived after 24 h incubation with all the three types of PSs. Compared with TPE-

IQ and TPE-IQ-2O, LIQ-TPE is more favourable with better biocompatibility on both MRC-5 and BHK-21 cells, and more than 85% of cells survived when incubating MRC-5 or BHK-21 cells with 5 μM LIQ-TPE for 24 h. The good biocompatibility of these PSs was beneficial for their practical applications.

Morphology study

To evaluate whether TPE-IQ, TPE-IQ-2O and LIQ-TPE could be used for the PDI of viruses, we first investigated the morphology changes of cells upon incubation with PS-treated viruses using an inverted microscope. In this experiment, foot-and-mouth disease virus (FMDV) and its host BHK-21 cells were employed. As shown in Fig. 2, without FMDV infection (cell only), BHK-21 cells were in the healthy state with a uniform spindle shape, and were polarity arranged without any cytopathic effects (CPEs). When BHK-21 cells were inoculated with the FMDV, the CPE was clearly observed after 24 h post-infection (h.p.i) with the FMDV, suggesting the successful infection of BHK-21 cells by the FMDV. When the FMDV was exposed to different concentrations of TPE-IQ, TPE-IQ-2O and LIQ-TPE in the dark, the CPE was still observed on all the three PS-treated cells at low concentrations, while in the presence of high concentrations of these PSs, the CPE was significantly decreased. These results suggested that PSs in the dark could inactivate the FMDV. When the FMDV was exposed to 9 mW cm^{-2} white light for 20 min in the presence of 0.5 μM TPE-IQ, TPE-IQ-2O and LIQ-TPE, a greatly reduced CPE was observed. Upon increasing the concentrations of PSs from 0.5 μM to 10 μM , the CPE decreased dramatically. As shown in Fig. 2, BHK-21 cells displayed almost no CPE after 24 h.p.i with the FMDV treated with 10 μM PSs and white-light irradiation. This cell morphology experiment proved that the ROS sensitized by TPE-IQ, TPE-IQ-2O and LIQ-TPE could effectively inactivate the FMDV and thus prevent BHK-21 cells from being infected.

qPCR for evaluating viral RNA copies in host cells

Next, the PDI performance was evaluated by using the real-time quantitative polymerase chain reaction (qPCR) for viral RNA

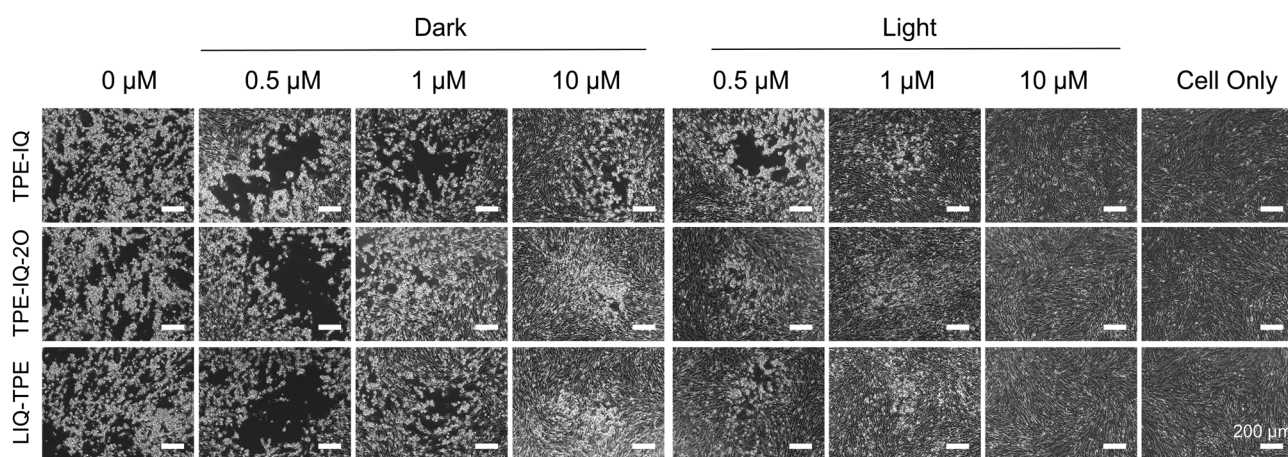


Fig. 2 Morphology study of BHK-21 cells infected by FMDV without/with isoquinolinium-based PS treatment. Prior to the infection of BHK-21 cells, FMDV was incubated with different concentrations of TPE-IQ, TPE-IQ-2O or LIQ-TPE for 20 min and then irradiated with white light or stored in the dark for 20 min. The morphological changes were recorded using a microscope after 24 h of incubation.



copies in host cells. FMDV, HCoV-OC43 and HCoV-229E were incubated with different concentrations of three PSs for 10 min, and then treated with 9 mW cm⁻² white-light irradiation or kept in the dark for 20 min. Subsequently, these viruses were employed to infect host cells (BHK-21 cells for FMDV, and MRC-5 cells for HCoV-OC43 and HCoV-229E). After incubation for 24 h, the total RNA from the infected cells was extracted and the level of viral RNA was measured by the qPCR (Table S1, ESI†). As shown in Fig. 3a–c, these three PSs exerted some dark toxicity towards the three viruses. Among all the three tested PSs, LIQ-TPE showed the best antiviral performance with lowest levels of viral RNA in all the three viruses, and the relative viral RNA expression levels for FMDV, HCoV-OC43 and HCoV-229E in the corresponding host cells were 60.6%, 54.0%, and 46.9%, respectively, after treatment with a high concentration of LIQ-TPE (10 μM) in the dark. Under light irradiation, the viral RNA was significantly decreased compared with their dark control group, and almost all the relative RNA expression levels of the three viruses were decreased to zero after treatment with 10 μM TPE-IQ, TPE-IQ-2O or LIQ-TPE, respectively. Compared with TPE-IQ and TPE-IQ-2O, LIQ-TPE showed a better antiviral performance. At a LIQ-TPE concentration of 1 μM and in the presence of white-light irradiation, the relative RNA expression levels were decreased to 12.3% and 5.5% for FMDV and HCoV-OC43, respectively, while the relative RNA expression level of

HCoV-229E was almost decreased to 0. For TPE-IQ, the relative RNA expression levels were 76.2%, 79.9% and 71.1% for FMDV, HCoV-OC43 and HCoV-229E, respectively, while for TPE-IQ-2O, the relative RNA expression levels were 51.2%, 51.2% and 30.1% for FMDV, HCoV-OC43 and HCoV-229E, respectively. Compared with the FMDV, the coronavirus such as HCoV-OC43 or HCoV-229E was more sensitive to these PSs. With the same treatment of PSs and light irradiation, HCoV-OC43 and HCoV-229E exhibited much lower relative RNA expression levels than the FMDV. This could be ascribed to the envelope structures of human coronaviruses, which encircled their capsid and genetic materials.^{46–48} The amphiphilic lipid bilayer in the envelope can provide extra binding sites for these three lipophilic isoquinolinium-based PSs through hydrophobic and electrostatic interactions.^{49–51} Therefore, these PSs demonstrated great potential in the inactivation of viruses through PDI, especially LIQ-TPE.

PDI effects of TPE-IQ, TPE-IQ-2O and LIQ-TPE on the levels of viral proteins in host cells

The presence of core protein in cells is regarded as a sign of virus infection.⁵² Taking the FMDV as an example, the FMDV 3D protein is a virus-encoded RNA-dependent RNA polymerase, which serves as the catalytic component in RNA replication and plays important roles in the life cycle of RNA viruses.⁵³

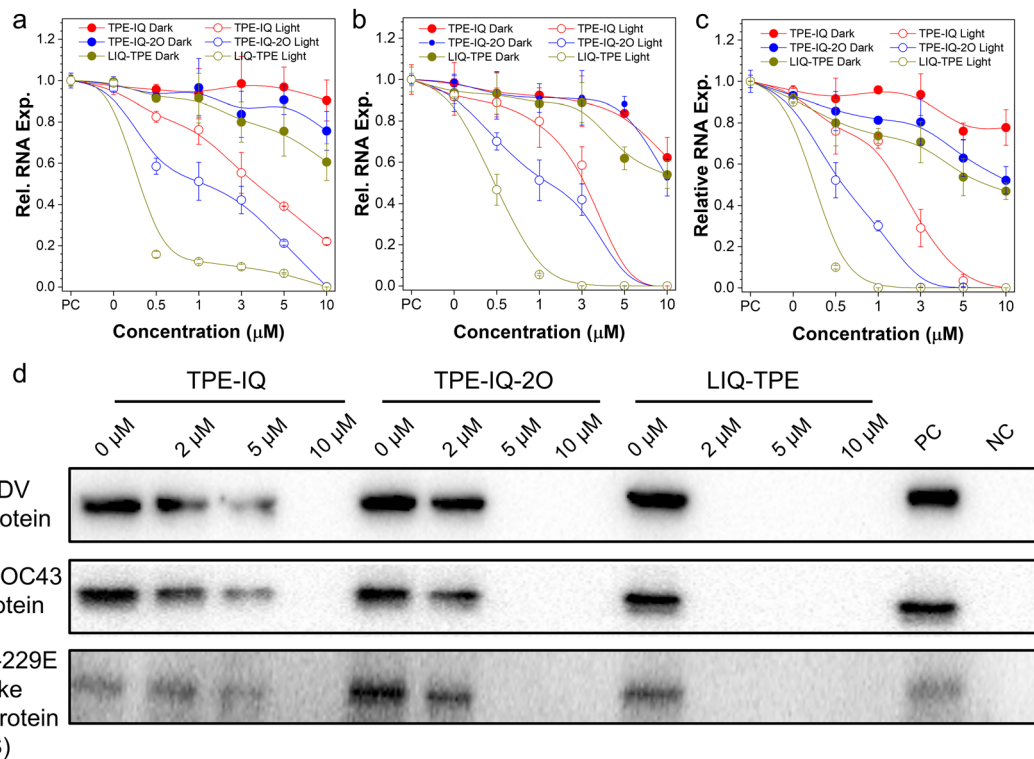


Fig. 3 (a–c) qPCR studies of the relative RNA expression of (a) FMDV, (b) HCoV-OC43, and (c) HCoV-229E. The viruses were treated with different concentrations of TPE-IQ, TPE-IQ-2O or LIQ-TPE for 20 min, irradiated with white-light irradiation or stored in the dark for 20 min, followed by infecting host cells and RNA extraction. The data were expressed as mean \pm SE and the number of duplicates is 3. (d) Western blot analysis of protein levels in host cells. Prior to incubation with host cells, viruses were treated with different concentrations of TPE-IQ, TPE-IQ-2O or LIQ-TPE (0, 2.0, 5.0, and 10.0 μM) for 20 min and then irradiated with white light for 20 min. PC: positive control, the host cells were infected with viruses without any treatment. NC: negative control, the host cells were not infected with viruses.

We examined the levels of the FMDV 3D protein by the Western blot assay after the PDI of the FMDV with these isoquinolinium-based PSs. After treating with different concentrations of PSs for 10 min and then irradiating with white light for 20 min, 2.5×10^{-4} PFU per cell-FMDV was incubated with BHK-21 cells for 24 h. Afterwards, the cells were harvested and lysed, and the FMDV 3D protein was analyzed from cell lysates by Western blot. As illustrated in Fig. 3d and Fig. S4 (ESI[†]), in the positive control group without PDI treatment, the band corresponding to the FMDV 3D protein could be clearly observed, while in the negative control group without the FMDV infection the band corresponding to the FMDV 3D protein was not detected. Meanwhile, the 3D protein gradually decreased as the concentration of PSs was increased from 0 μM to 10 μM . It is worth noting that almost no 3D protein was detected when the FMDV was treated with 2 μM LIQ-TPE and white-light irradiation. These results demonstrated the effective inactivation of the FMDV through PDI and loss of their invading ability. Following similar experimental procedures, we also examined the HCoV-OC43 N protein (Fig. 3d and Fig. S5, ESI[†]) and HCoV-229E spike glycoprotein (S) levels (Fig. 3d and Fig. S6, ESI[†]) in MRC-5 cells. Both the HCoV-OC43 N protein and HCoV-229E spike

glycoprotein (S) levels were decreased gradually as PS concentrations were elevated, which was similar to that observed in the FMDV. Among the three PSs, LIQ-TPE demonstrated the best antiviral performance. The good PDI performance of these PSs makes them excellent candidates for practical applications.

The expression levels of FMDV, HCoV-OC43 and HCoV-229E proteins

Protein expression is another important process for virus infection.⁵⁴ The immunofluorescence assay was used to investigate the expression levels of FMDV, HCoV-OC43 and HCoV-229E proteins in host cells. After treatment with PSs and light irradiation, the FMDV and HCoV-OC43/HCoV-229E were used to infect BHK-21 cells and MRC-5 cells, respectively, which were then subjected to incubation for 24 h. Subsequently, the BHK-21 cells were immunostained with the FMDV 3D rabbit primary antibody and FITC-tagged goat anti-rabbit IgG (H+L) secondary antibody, while the MRC-5 cells inoculated with HCoV-OC43 were subjected to immunostaining with the anti-coronavirus mouse primary antibody and TRITC-tagged goat anti-mouse IgG (H+L) secondary antibody and MRC-5 incubated with HCoV-229E was treated with the HCoV-229E spike glycoprotein (S) rabbit primary antibody and

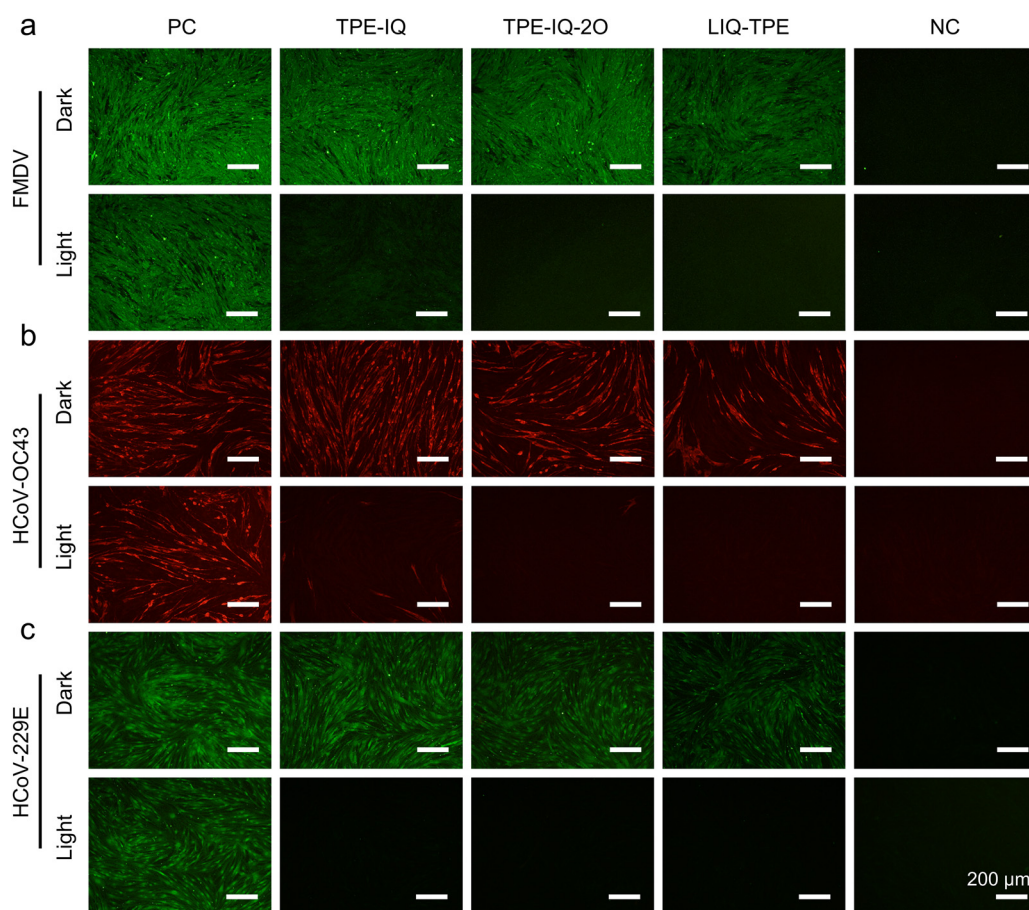


Fig. 4 (a and b) Immunofluorescence studies of (a) BHK-21 cells infected with the FMDV and (b and c) MRC-5 cells infected with (b) HCoV-OC43 and (c) HCoV-229E, which were pre-treated with 5 μM TPE-IQ, TPE-IQ-20 or LIQ-TPE and then subjected to irradiation with white light or storage in the dark for 20 min. PC: the host cells were infected with the untreated virus. NC: the host cells were not infected with the virus. Green channel: λ_{ex} : 460–490 nm, λ_{ex} : 520–750 nm; red channel: λ_{ex} : 510–550 nm, λ_{ex} : 570–750 nm. Scale bar: 200 μm .



FITC-tagged goat anti-rabbit IgG (H+L) secondary antibody. As shown in Fig. 4a, after the treatment of the FMDV with 5 μM PSs and storage in the dark, the protein expression of the FMDV treated with TPE-IQ and TPE-IQ-2O was almost not changed, while BHK-21 cells incubated with the LIQ-TPE-treated FMDV showed the weakest green fluorescence among the three groups, suggesting that LIQ-TPE in the dark could partially inactivate the FMDV. In the presence of both PSs and white-light irradiation, almost no fluorescence from the virus antigen was observed, manifesting the excellent PDI performance of these PSs. For HCoV-OC43, incubation with TPE-IQ-2O and LIQ-TPE in the dark could partially inactivate HCoV-OC43 with reduced red fluorescence of TRITC (Fig. 4b). Treatment of HCoV-OC43 with both PSs and light irradiation could greatly elevate the inactivation efficacy, with almost no red fluorescence from immunofluorescence imaging. Similar experimental results were obtained when employing HCoV-229E to infect MRC-5, which confirmed their PDI effect on HCoV-229E (Fig. 4c). The results ambiguously proved that these isoquinolinium-based PSs could effectively inactivate the FMDV, HCoV-OC43 and HCoV-229E through PDI *in vitro*.

Viral titering-median tissue culture infectious dose (TCID_{50}) assay

We also conducted the TCID_{50} assay to quantify the number of infectious virus particles. After incubating the viruses with different concentrations of PSs in the presence of white light for 20 min, HCoV-OC43 and FMDV were incubated with the corresponding host cells for 3 days, followed by the quantification of the plaques formed. As shown in Fig. 5a–c, the $\log_{10}\text{TCID}_{50}$ decreased

gradually as the concentration of PSs was increased from 0 to 5 μM . At a PS concentration of 5 μM and with white-light irradiation, the $\log_{10}\text{TCID}_{50}$ values of HCoV-OC43 were decreased to 19.8% (TPE-IQ, Fig. 5a), 20.8% (TPE-IQ-2O, Fig. 5b) and 4.0% (LIQ-TPE, Fig. 5c) of the positive control group. Meanwhile, the $\log_{10}\text{TCID}_{50}$ values of the FMDV were significantly decreased to 17.2% (TPE-IQ, Fig. 5d), 16.4% (TPE-IQ-2O, Fig. 5e) and 4.3% (LIQ-TPE, Fig. 5f) of the positive control group. This TCID_{50} result clearly demonstrated the PDI effect of these isoquinolinium-based AIE-active PSs.

PDI of viruses on high-touch surfaces

As mentioned in the Introduction, AIE-active PSs are advantageous for the application in the solid state, due to their enhanced ROS sensitizing efficiency. This makes them ideal candidates for PDI of viruses on high-touch surfaces. To demonstrate the feasibility of employing these isoquinolinium-based PSs for the PDI of viruses on high-touch surfaces, different concentrations of these PSs in ethanol were dropped onto sterilized stainless steel and glass slides, and dried under air. Afterwards, these surfaces were immersed in virus-containing culture media, and exposed to white light or kept in the dark for 20 min. The virus-containing media were then acquired and co-cultured with corresponding host cells for 24 h, followed by the evaluation of the viral RNA levels in the infected cells with the qPCR.

As shown in Fig. 6, isoquinolinium-based PSs could efficiently inactivate all the three kinds of viruses on stainless steel or glass slides with white-light irradiation. All the three PSs could effectively inactivate the three viruses through PDI. When treated

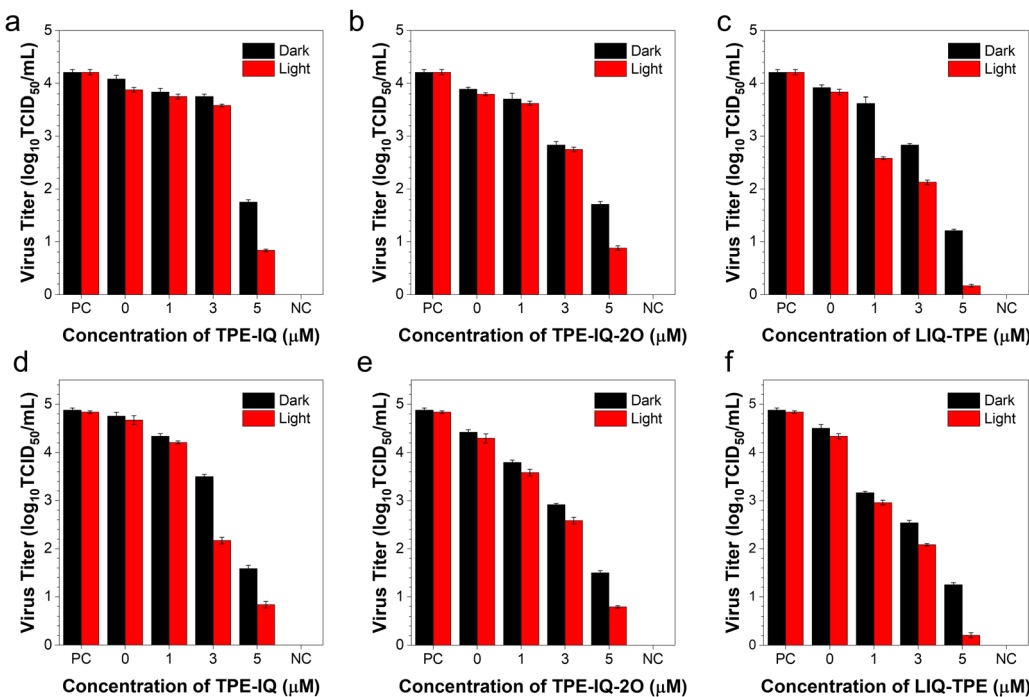


Fig. 5 TCID_{50} assay for detecting the infectious viral (a–c) HCoV-OC43 and (d–f) FMDV titers. The viruses were incubated with different concentrations of TPE-IQ, TPE-IQ-2O or LIQ-TPE without/with white-light irradiation for 20 min. PC: positive control, the host cells were infected with viruses. NC: negative control, the host cells were not infected with viruses. Data were expressed as mean \pm SE, and the number of duplicates is 10.



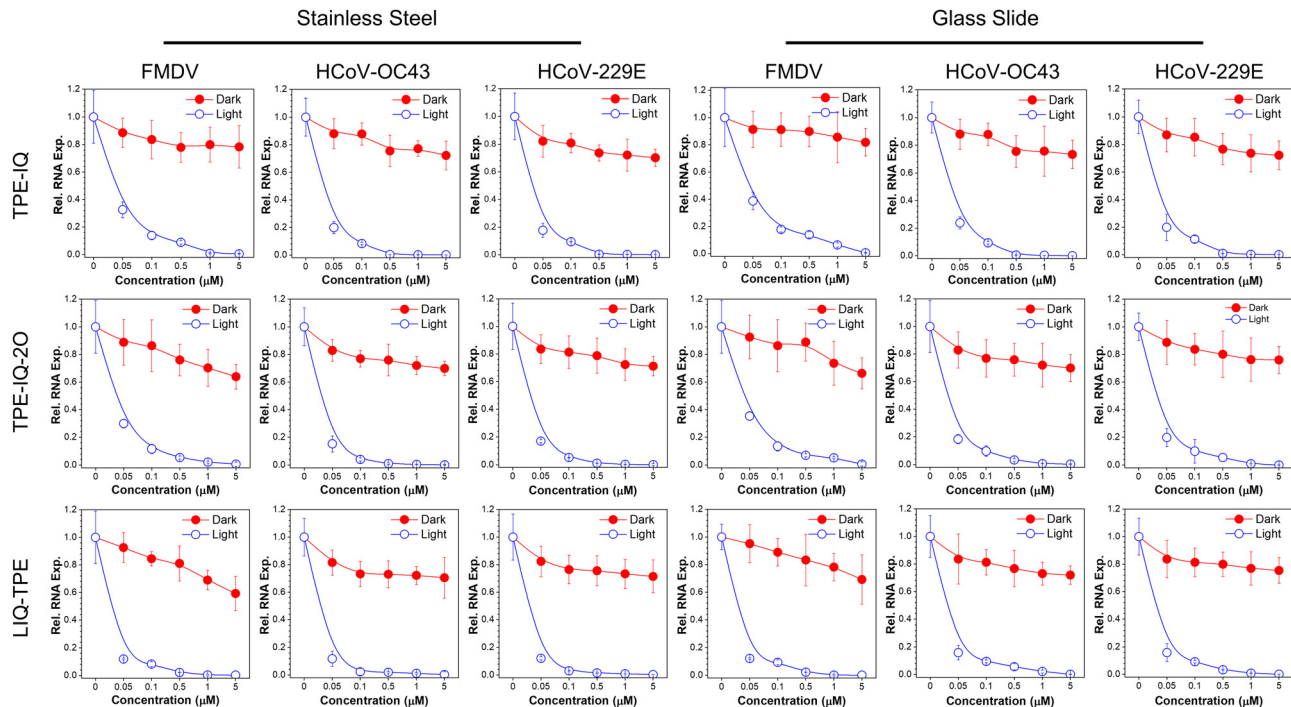


Fig. 6 PDI effects of TPE-IQ, TPE-IQ-2O and LIQ-TPE on the simulated high-touch surfaces of stainless steel or glass slides. Viruses were incubated with PSs on simulated high-touch surfaces without/with white-light irradiation for 20 min, followed by infection of their host cells for 24 h, extraction of RNA and qPCR analysis. Data were expressed as mean \pm SE, and the number of duplicates is 3.

in the dark, the relative RNA level remained at a relatively high level, while upon light irradiation, significantly decreased relative RNA levels were observed in all the tested groups. Among all the three PSs, LIQ-TPE demonstrated the best performance, with excellent PDI performance even at a low concentration of 0.05 μ M. At a LIQ-TPE concentration of 0.1 μ M, the relative RNA expression levels on stainless steel were decreased to 8.2%, 2.3% and 3.0% for FMDV, HCoV-OC43 and HCoV-229E, respectively. For glasses, the relative RNA expression levels were decreased to 9.3%, 9.6% and 9.2% for FMDV, HCoV-OC43 and HCoV-229E, respectively. When the concentration was increased to 1.0 μ M, the relative RNA expression levels were almost decreased to zero for the viruses on both stainless steel and glass slides. The other two PSs also showed good performance on the PDI of viruses. The PDI performance of these PSs on the simulated high-touch surface was better than that in culture media, which might be ascribed to the high ROS sensitizing efficiency in the aggregated state. The excellent performance of these AIE-active PSs for the PDI of viruses endows them with great potential for the photodynamic combat of SARS-CoV-2 by employing these photosensitizers to prevent the spread of infectious pathogens in public places.

Conclusions

In summary, three isoquinolinium-based PSs with aggregation-induced emission characteristics, namely TPE-IQ, TPE-IQ-2O and LIQ-TPE, were used for the photodynamic combat of viruses. These three PSs demonstrated good ROS sensitizing ability. Among them, LIQ-TPE demonstrated the highest ROS

sensitizing ability with a much higher $^1\text{O}_2$ sensitizing efficiency than the widely used PS, RB. Meanwhile, LIQ-TPE has the lowest cytotoxicity and the best antiviral performance compared with the other two PSs without light irradiation. Once treated with light, the three PSs could significantly decrease infectious ability of viruses through PDI of the tested viruses (FMDV, HCoV-OC43 and HCoV-229E), with greatly reduced RNA copies in host cells. The PDI effect of three PSs was confirmed by examining the protein levels using Western blot, immunofluorescence imaging of viral proteins and viral titer TCID_{50} . Among the three PSs, LIQ-TPE exhibited the best antiviral performance for all the tested viruses. Furthermore, these PSs were successfully employed in PDI of viruses in simulated high-touch surfaces with excellent performance, such as stainless steel or glass slides. Notably, all these PDI experiments were conducted at a low white-light intensity of 9 mW cm^{-2} , which was demonstrative of their promising practical applications. This work is expected to inspire new preventive strategies for combating COVID-19 and controlling the pandemic situation.

Conflicts of interest

There are no conflicts to declare.

Acknowledgements

S. C. acknowledges the start-up funding from Ming Wai Lau Centre for Reparative Medicine, Karolinska Institutet. E. Z. acknowledges financial support from the National Natural

Science Foundation of China (22005050). C. S. acknowledges financial support from the National Science and Technology Infrastructure Grants (NSTI-CR14-19) and the Science and Technology Innovation Grants of Hubei province (2021CFB357). M.-Y. W. acknowledges financial support from the National Natural Science Foundation of China (22177094).

Notes and references

1 P. Zhou, X. Lou Yang, X. G. Wang, B. Hu, L. Zhang, W. Zhang, H. R. Si, Y. Zhu, B. Li, C. L. Huang, H. D. Chen, J. Chen, Y. Luo, H. Guo, R. Di Jiang, M. Q. Liu, Y. Chen, X. R. Shen, X. Wang, X. S. Zheng, K. Zhao, Q. J. Chen, F. Deng, L. L. Liu, B. Yan, F. X. Zhan, Y. Y. Wang, G. F. Xiao and Z. L. Shi, A pneumonia outbreak associated with a new coronavirus of probable bat origin, *Nature*, 2020, **579**, 270–273.

2 F. Wu, S. Zhao, B. Yu, Y. M. Chen, W. Wang, Z. G. Song, Y. Hu, Z. W. Tao, J. H. Tian, Y. Y. Pei, M. L. Yuan, Y. L. Zhang, F. H. Dai, Y. Liu, Q. M. Wang, J. J. Zheng, L. Xu, E. C. Holmes and Y. Z. Zhang, A new coronavirus associated with human respiratory disease in China, *Nature*, 2020, **579**, 265–269.

3 A. E. Gorbatenko, S. C. Baker, R. S. Baric, R. J. de Groot, C. Drosten, A. A. Gulyaeva, B. L. Haagmans, C. Lauber, A. M. Leontovich, B. W. Neuman, D. Penzar, S. Perlman, L. L. M. Poon, D. V. Samborskiy, I. A. Sidorov, I. Sola and J. Ziebuhr, The species Severe acute respiratory syndrome-related coronavirus: classifying 2019-nCoV and naming it SARS-CoV-2, *Nat. Microbiol.*, 2020, **5**, 536–544.

4 Y. Cao, J. Wang, F. Jian, T. Xiao, W. Song, A. Yisimayi, W. Huang, Q. Li, P. Wang, R. An, J. Wang, Y. Wang, X. Niu, S. Yang, H. Liang, H. Sun, T. Li, Y. Yu, Q. Cui, S. Liu, X. Yang, S. Du, Z. Zhang, X. Hao, F. Shao, R. Jin, X. Wang, J. Xiao, Y. Wang and X. S. Xie, Omicron escapes the majority of existing SARS-CoV-2 neutralizing antibodies, *Nature*, 2022, **602**, 657–663.

5 B. Vellingiri, K. Jayaramayya, M. Iyer, A. Narayanasamy, V. Govindasamy, B. Giridharan, S. Ganesan, A. Venugopal, D. Venkatesan, H. Ganesan, K. Rajagopalan, P. K. S. M. Rahman, S. G. Cho, N. S. Kumar and M. D. Subramaniam, COVID-19: A promising cure for the global panic, *Sci. Total Environ.*, 2020, **725**, 138277.

6 A. Widders, A. Broom and J. Broom, SARS-CoV-2: The viral shedding vs infectivity dilemma, *Infect. Dis. Health*, 2020, **25**, 210–215.

7 W. A. Rutala, D. J. Weber and the Healthcare Infection Control Practices Advisory Committee, Guideline for Disinfection and Sterilization in Healthcare Facilities, 2008.

8 L. Dietz, P. F. Horve, D. A. Coil, M. Fretz, J. A. Eisen and K. Van Den Wymelenberg, 2019 Novel Coronavirus (COVID-19) Pandemic: Built Environment Considerations To Reduce Transmission Leslie, *mSystems*, 2020, **5**, e00245–e00320.

9 S. M. Imani, L. Ladouceur, T. Marshall, R. MacLachlan, L. Soleymani and T. F. Didar, Antimicrobial nanomaterials and coatings: Current mechanisms and future perspectives to control the spread of viruses including SARS-CoV-2, *ACS Nano*, 2020, **14**, 12341–12369.

10 E. Kim, E. K. Lim, G. Park, C. Park, J. W. Lim, H. Lee, W. Na, M. Yeom, J. Kim, D. Song and S. Haam, Advanced Nanomaterials for Preparedness Against (Re-)Emerging Viral Diseases, *Adv. Mater.*, 2021, **33**, 2005927.

11 V.-N. Nguyen, Z. Zhao, B. Z. Tang and J. Yoon, Organic photosensitizers for antimicrobial phototherapy, *Chem. Soc. Rev.*, 2022, **51**, 3324–3340.

12 Z. Zhang, M. Kang, H. Tan, N. Song, M. Li, P. Xiao, D. Yan, L. Zhang, D. Wang and B. Z. Tang, The fast-growing field of photo-driven theranostics based on aggregation-induced emission, *Chem. Soc. Rev.*, 2022, **51**, 1983–2030.

13 T. C. Pham, V. N. Nguyen, Y. Choi, S. Lee and J. Yoon, Recent Strategies to Develop Innovative Photosensitizers for Enhanced Photodynamic Therapy, *Chem. Rev.*, 2021, **121**, 13454–13619.

14 D. E. J. G. J. Dolmans, D. Fukumura and R. K. Jain, Photodynamic therapy for cancer, *Nat. Rev. Cancer*, 2003, **3**, 380–387.

15 V. N. Nguyen, Y. Yan, J. Zhao and J. Yoon, Heavy-Atom-Free Photosensitizers: From Molecular Design to Applications in the Photodynamic Therapy of Cancer, *Acc. Chem. Res.*, 2021, **54**, 207–220.

16 Y. Xu, R. Xu, Z. Wang, Y. Zhou, Q. Shen, W. Ji, D. Dang, L. Meng and B. Z. Tang, Recent advances in luminescent materials for super-resolution imaging: Via stimulated emission depletion nanoscopy, *Chem. Soc. Rev.*, 2021, **50**, 667–690.

17 P. Xiao, Z. Shen, D. Wang, Y. Pan, Y. Li, J. Gong, L. Wang, D. Wang and B. Z. Tang, Precise Molecular Engineering of Type I Photosensitizers with Near-Infrared Aggregation-Induced Emission for Image-Guided Photodynamic Killing of Multidrug-Resistant Bacteria, *Adv. Sci.*, 2022, **9**, 2104079.

18 T. Zhou, R. Hu, L. Wang, Y. Qiu, G. Zhang, Q. Deng, H. Zhang, P. Yin, B. Situ, C. Zhan, A. Qin and B. Z. Tang, An AIE-Active Conjugated Polymer with High ROS-Generation Ability and Biocompatibility for Efficient Photodynamic Therapy of Bacterial Infections, *Angew. Chem., Int. Ed.*, 2020, **59**, 9952–9956.

19 J. B. Birks, *Photophysics of Aromatic Molecules*, Wiley, New York, 1970, vol. 704.

20 G. Feng, G. Q. Zhang and D. Ding, *Chem. Soc. Rev.*, 2020, **49**, 8179–8234.

21 Z. Guo, C. Yan and W. H. Zhu, High-Performance Quinoline-Malononitrile Core as a Building Block for the Diversity-Oriented Synthesis of AIEgens, *Angew. Chem., Int. Ed.*, 2020, **59**, 9812–9825.

22 W. Yao, M. Tebyetekerwa, X. Bian, W. Li, S. Yang, M. Zhu, R. Hu, Z. Wang, A. Qin and B. Z. Tang, Materials interaction in aggregation-induced emission (AIE)-based fluorescent resin for smart coatings, *J. Mater. Chem. C*, 2018, **6**, 12849–12857.

23 L. Wang, L. Wang, X. Yang, W. Li, L. Chen, J. Tang, W. Cong, R. Hu, M. Tebyetekerwa and B. Tang, Aggregation-induced emission molecules enable characterization of superhydrophobic coatings, *Prog. Org. Coat.*, 2022, **163**, 106633.

24 J. Luo, Z. Xie, Z. Xie, J. W. Y. Lam, L. Cheng, H. Chen, C. Qiu, H. S. Kwok, X. Zhan, Y. Liu, D. Zhu and B. Z. Tang,



Aggregation-induced emission of 1-methyl-1,2,3,4,5-pentaphenylsilole, *Chem. Commun.*, 2001, 1740–1741.

25 M. Y. Wu, J. K. Leung, L. Liu, C. Kam, K. Y. K. Chan, R. A. Li, S. Feng and S. Chen, A Small-Molecule AIE Chromosome Periphery Probe for Cytogenetic Studies, *Angew. Chem., Int. Ed.*, 2020, **59**, 10327–10331.

26 X. Cai and B. Liu, Aggregation-Induced Emission: Recent Advances in Materials and Biomedical Applications, *Angew. Chem., Int. Ed.*, 2020, **59**, 9868–9886.

27 J. Li, Y. Zhang, P. Wang, L. Yu, J. An, G. Deng, Y. Sun and J. Seung Kim, Reactive oxygen species, thiols and enzymes activatable AIEgens from single fluorescence imaging to multi-functional theranostics, *Coord. Chem. Rev.*, 2021, **427**, 213559.

28 W. Xu, D. Wang and B. Z. Tang, NIR-II AIEgens: A Win-Win Integration towards Bioapplications, *Angew. Chem., Int. Ed.*, 2021, **60**, 7476–7487.

29 W. Li, Y. Ding, M. Tebyetekerwa, Y. Xie, L. Wang, H. Li, R. Hu, Z. Wang, A. Qin and B. Z. Tang, Fluorescent aggregation-induced emission (AIE)-based thermosetting electrospun nanofibers: fabrication, properties and applications, *Mater. Chem. Front.*, 2019, **3**, 2491–2498.

30 Z. Zhao, H. Zhang, J. W. Y. Lam and B. Z. Tang, Aggregation-Induced Emission: New Vistas at the Aggregate Level, *Angew. Chem., Int. Ed.*, 2020, **59**, 9888–9907.

31 C. Xu, R. Ye, H. Shen, J. W. Y. Lam, Z. Zhao and B. Z. Tang, Molecular Motion and Nonradiative Decay: Towards Efficient Photothermal and Photoacoustic Systems, *Angew. Chem., Int. Ed.*, 2022, **61**, e202204604.

32 X. He, L. H. Xiong, Z. Zhao, Z. Wang, L. Luo, J. W. Y. Lam, R. T. K. Kwok and B. Z. Tang, *Theranostics*, 2019, **9**, 3223–3248.

33 M. Gu, S. Jiang, X. Xu, M. Wu, C. Chen, Y. Yuan, Q. Chen, Y. Sun, L. Chen, C. Shen, P. Guo, S. Liu, E. Zhao, S. Chen and S. Chen, Simultaneous Photodynamic Eradication of Tooth Biofilm and Tooth Whitening with an Aggregation-Induced Emission Luminogen, *Adv. Sci.*, 2022, 2106071.

34 A. Wiehe, J. M. O'brien and M. O. Senge, Trends and targets in antiviral phototherapy, *Photochem. Photobiol. Sci.*, 2019, **18**, 2565–2612.

35 N. Kipshidze, N. Yeo and N. Kipshidze, Photodynamic therapy for COVID-19, *Nat. Photonics*, 2020, **14**, 651–652.

36 M. Y. Wu, M. Gu, J. K. Leung, X. Li, Y. Yuan, C. Shen, L. Wang, E. Zhao and S. Chen, A Membrane-Targeting Photosensitizer with Aggregation-Induced Emission Characteristics for Highly Efficient Photodynamic Combat of Human Coronaviruses, *Small*, 2021, **17**, 2101770.

37 C. Zhou, C. Peng, C. Shi, M. Jiang, J. H. C. Chau, Z. Liu, H. Bai, R. T. K. Kwok, J. W. Y. Lam, Y. Shi and B. Z. Tang, Mitochondria-Specific Aggregation-Induced Emission Lumogens for Selective Photodynamic Killing of Fungi and Efficacious Treatment of Keratitis, *ACS Nano*, 2021, **15**, 12129–12139.

38 K. Chen, P. He, Z. Wang and B. Z. Tang, A Feasible Strategy of Fabricating Type i Photosensitizer for Photodynamic Therapy in Cancer Cells and Pathogens, *ACS Nano*, 2021, **15**, 7735–7743.

39 C. Zhou, M. Jiang, J. Du, H. Bai, G. Shan, R. T. K. Kwok, J. H. C. Chau, J. Zhang, J. W. Y. Lam, P. Huang and B. Z. Tang, One stone, three birds: One AIEgen with three colors for fast differentiation of three pathogens, *Chem. Sci.*, 2020, **11**, 4730–4740.

40 L. Liu, Q. Zou, J. K. Leung, J. L. Wang, C. Kam, S. Chen, S. Feng and M. Y. Wu, Ultrafast labeling and high-fidelity imaging of mitochondria in cancer cells using an aggregation-enhanced emission fluorescent probe, *Chem. Commun.*, 2019, **55**, 14681–14684.

41 M. Y. Wu, L. Liu, Q. Zou, J. K. Leung, J. L. Wang, T. Y. Chou and S. Feng, Simple synthesis of multifunctional photosensitizers for mitochondrial and bacterial imaging and photodynamic anticancer and antibacterial therapy, *J. Mater. Chem. B*, 2020, **8**, 9035–9042.

42 E. Zhao, H. Deng, S. Chen, Y. Hong, C. W. T. Leung, J. W. Y. Lam and B. Z. Tang, A dual functional AEE fluorogen as a mitochondrial-specific bioprobe and an effective photosensitizer for photodynamic therapy, *Chem. Commun.*, 2014, **50**, 14451–14454.

43 C. Gui, E. Zhao, R. T. K. Kwok, A. C. S. Leung, J. W. Y. Lam, M. Jiang, H. Deng, Y. Cai, W. Zhang, H. Su and B. Z. Tang, AIE-active theranostic system: selective staining and killing of cancer cells, *Chem. Sci.*, 2017, **8**, 1822–1830.

44 Q. Zou, J. L. Wang, M. Y. Wu, C. Kam, S. Y. Lee, S. Feng and S. Chen, A Highly Efficient Aggregation-induced Emission Photosensitizer for Photodynamic Combat of Multidrug-resistant Bacteria, *Chem. Res. Chin. Univ.*, 2021, **37**, 150–156.

45 Y. Yuan, G. Feng, W. Qin, B. Z. Tang and B. Liu, Targeted and image-guided photodynamic cancer therapy based on organic nanoparticles with aggregation-induced emission characteristics, *Chem. Commun.*, 2014, **50**, 8757–8760.

46 P. Zimmermann and N. Curtis, Coronavirus infections in children including COVID-19: An overview of the epidemiology, clinical features, diagnosis, treatment and prevention options in children, *J. Pediatr. Infect. Dis. Soc.*, 2020, **39**, 355–368.

47 F. Käsermann and C. Kempf, Photodynamic inactivation of enveloped viruses by buckminsterfullerene1For the described inactivation procedure, a patent application was submitted.1, *Antiviral Res.*, 1997, **34**, 65–70.

48 M. Lorizate and H. G. Kräusslich, Role of lipids in virus replication, *Cold Spring Harbor Perspect. Biol.*, 2011, **3**, a004820.

49 M. Y. Wu, A. Y. H. Wong, J. K. Leung, C. Kam, K. Lap-Kei Wu, Y. S. Chan, K. Liu, N. Y. Ip and S. Chen, A near-infrared AIE fluorescent probe for myelin imaging: From sciatic nerve to the optically cleared brain tissue in 3D, *Proc. Natl. Acad. Sci. U. S. A.*, 2021, **118**, e2106143118.

50 M.-Y. Wu, J.-K. Leung, C. Kam, T. Y. Chou, J.-L. Wang, X. Zhao, S. Feng and S. Chen, A near-infrared plasma membrane-specific AIE probe for fluorescence lifetime imaging of phagocytosis, *Sci. China: Chem.*, 2022, **65**, 979–988.

51 M. Y. Wu, J. K. Leung, C. Kam, B. Situ, Z. J. Wu, T. Y. Chou, S. Feng and S. Chen, Cancer cell-selective aggregation-induced emission probe for long-term plasma membrane imaging, *Cell Rep. Phys. Sci.*, 2022, **3**, 100735.

52 R. Kumar, M. Hosamani, B. P. Sreenivasa, A. Kotyal and R. Venkataramanan, Expression of foot-and-mouth disease



virus non-structural protein, 3D in insect cells and its application in detection of anti-fmdv antibodies, *Indian J. Virol.*, 2012, **23**, 326–332.

53 C. Ferrer-Orta, R. Agudo, E. Domingo and N. Verdaguer, Structural insights into replication initiation and elongation processes by the FMDV RNA-dependent RNA polymerase, *Curr. Opin. Struct. Biol.*, 2009, **19**, 752–758.

54 D. M. Ozata, I. Gainetdinov, A. Zoch, D. O'Carroll and P. D. Zamore, PIWI-interacting RNAs: small RNAs with big functions, *Nat. Rev. Genet.*, 2019, **20**, 89–108.

